OPEN ACCESS



Ly α Halo Properties and Dust in the Circumgalactic Medium of $z\sim 2$ Star-forming Galaxies

Zhiyuan Song¹, Naveen A. Reddy¹, Yuguang Chen^{2,3}, Alice E. Shapley⁴, Saeed Rezaee¹, Andrew Weldon¹, Tara Fetherolf⁵, Alison L. Coil⁶, Bahram Mobasher¹, and Charles C. Steidel²

Department of Physics and Astronomy, University of California, Riverside, 900 University Avenue, Riverside, CA 92521, USA; zhiyuan.song@email.ucr.edu

² Cahill Center for Astronomy and Astrophysics, California Institute of Technology, MC249-17, Pasadena, CA 91125, USA

³ Department of Physics and Astronomy, University of California Davis, 1 Shields Avenue, Davis, CA 95616, USA

⁴ Department of Physics and Astronomy, University of California, Los Angeles, CA 90095, USA

⁵ Department of Earth and Planetary Sciences, University of California, Riverside, CA 92521, USA

⁶ Center for Astrophysics and Space Sciences, University of California, 9500 Gilman Drive, La Jolla, CA 92093, USA

**Received 2023 November 22; revised 2024 April 23; accepted 2024 May 7; published 2024 July 8

Abstract

We present Keck Cosmic Web Imager integral-field unit observations around extended Ly α halos of 27 typical star-forming galaxies with redshifts 2.0 < z < 3.2 drawn from the MOSFIRE Deep Evolution Field survey. We examine the average Ly α surface brightness profiles in bins of star formation rate (SFR), stellar mass (M_*), age, stellar continuum reddening, SFR surface density ($\Sigma_{\rm SFR}$), and $\Sigma_{\rm SFR}$ normalized by stellar mass ($\Sigma_{\rm sSFR}$). The scale lengths of the halos correlate with stellar mass, age, and stellar continuum reddening and anticorrelate with SFR, $\Sigma_{\rm SFR}$, and $\Sigma_{\rm sSFR}$. These results are consistent with a scenario in which the down-the-barrel fraction of Ly α emission is modulated by the low-column-density channels in the interstellar medium, and in which the neutral gas covering fraction increases with stellar mass, age, and E(B-V) and decreases with SFR, $\Sigma_{\rm SFR}$, and $\Sigma_{\rm sSFR}$. We also find that the resonantly scattered Ly α emission suffers greater attenuation than the (nonresonant) stellar continuum emission, and that the difference in attenuation increases with stellar mass, age, and stellar continuum reddening, and decreases with $\Sigma_{\rm sSFR}$. These results imply that more reddened galaxies have more dust in their circumgalactic medium.

Unified Astronomy Thesaurus concepts: Galaxy evolution (594); Interstellar medium (847); High-redshift galaxies (734)

1. Introduction

Recent observations indicate that extended Ly α halos are ubiquitous around high-redshift galaxies, based on both stacked images (Steidel et al. 2011; Matsuda et al. 2012; Feldmeier et al. 2013; Momose et al. 2014, 2016; Xue et al. 2017) and individual detections (Wisotzki et al. 2016; Leclercq et al. 2017; Erb et al. 2018, 2023). There are several scenarios that might explain diffuse halos of Ly α emission. These include resonant scattering of Ly α photons produced in star-forming regions and/or active galactic nuclei (AGNs; Meier & Terlevich 1981; Dijkstra et al. 2006; Steidel et al. 2011; Zheng et al. 2011; Dijkstra & Kramer 2012; Orsi et al. 2012), Ly α emission powered by the loss of gravitational energy by inflowing gas (Dijkstra & Loeb 2009; Faucher-Giguère et al. 2010; Goerdt et al. 2010; Rosdahl & Blaizot 2012; Lake et al. 2015), and Ly α fluorescence due to a nearby ionizing source unrelated to the galaxy (Adelberger et al. 2006; Mas-Ribas & Dijkstra 2016). The prevalence of Ly α halos irrespective of the large-scale environment and the large inferred covering fraction of outflowing gas suggests that, for the most part, these halos reflect the resonant scattering of Ly α photons originating from the sites of star formation within galaxies (Momose et al. 2014; Byrohl et al. 2021; Kikuta et al. 2023).

Original content from this work may be used under the terms of the Creative Commons Attribution 4.0 licence. Any further distribution of this work must maintain attribution to the author(s) and the title of the work, journal citation and DOI.

The relation between the sizes of extended Ly α halos and their host galaxies has been investigated in several studies. Previous studies found that the scale length of the Ly α halo is positively correlated with the total Ly α luminosity and UV magnitude, but independent of the Ly α equivalent width (Steidel et al. 2011; Leclercq et al. 2017; Xue et al. 2017). However, Momose et al. (2016) found that the scale length is anticorrelated with the Ly α luminosity and rest-frame equivalent width, while the influence of UV magnitude remains unclear. The link between the Ly α halo size and the UV magnitude of the host galaxy may indicate that star formation rate (SFR) plays an important role in powering extended Ly α emission, which favors the resonant scattering origin of the Ly α emission. On the other hand, supernovae and/or stellar winds could also regulate the Ly α halo by carving low-columndensity channels in the interstellar medium (ISM) and the circumgalactic medium (CGM) (Gnedin et al. 2008; Zackrisson et al. 2013; Ma et al. 2016, 2020; Kimm et al. 2019; Kakiichi & Gronke 2021). The channels would ease the escape of Ly α photons at small impact parameters (Reddy et al. 2016), hence reducing the scale length. Such competing mechanisms together may explain why Momose et al. (2016) found no correlation between UV magnitude and Ly α halo scale length.

While these studies focused on the UV properties of host galaxies, there has been little investigation into how the sizes and shapes of halos scale with the properties of host galaxies, including stellar mass and reddening. Yet, it is perhaps reasonable to think that these halos, which effectively trace the gas content around galaxies, may depend on the maturity

(i.e., the stellar mass, age, and reddening) of their host galaxies. Many works have shown that the H I covering fraction is a key parameter for Ly α escape (Kornei et al. 2010; Hayes et al. 2011; Wofford et al. 2013; Borthakur et al. 2014; Rivera-Thorsen et al. 2015; Trainor et al. 2015; Reddy et al. 2016, 2022; Steidel et al. 2018; Jaskot et al. 2019). Since stellar feedback could modulate the HI covering fraction by creating low-column-density channels in the ISM and the CGM (Gnedin et al. 2008; Ma et al. 2016, 2020; Kimm et al. 2019; Kakiichi & Gronke 2021), it is important to investigate the impact of the SFR surface density on the escape of Ly α photons. Reddy et al. (2022) also found that the galaxy potential plays an important role in the escape of Ly α photons. However, measuring these quantities requires deep multiwavelength photometric and spectroscopic observations, which were lacking in previous studies (e.g., Wisotzki et al. 2016).

Detecting diffuse Ly α halos around high-redshift galaxies is challenging since it requires high sensitivity and adequate spatial resolution. The state-of-the-art integral-field unit (IFU) instrument Keck Cosmic Web Imager (KCWI; Morrissey et al. 2018) was designed to detect such halos around typical star-forming galaxies at z > 2.0 (Martin et al. 2010; Morrissey et al. 2012; Chen et al. 2021). KCWI has a wavelength coverage of 3500–5600 Å and a spectral resolution of $R \sim 1800$ (for a medium slicer and BL grating configuration) for the blue channel. While the Multi-unit Spectroscopic Explorer (MUSE; Bacon et al. 2010) offers a larger field of view, KCWI's unparalleled blue sensitivity enables observations of Ly α halos at lower redshifts, where surface brightness dimming is mitigated and the sky background is low.

In this paper, we investigate the relations between the properties of Ly α halos and the physical properties of their host galaxies using KCWI IFU data of a sample of 27 galaxies at redshifts 2.0 < z < 3.2. These galaxies are selected from the MOSFIRE Deep Evolution Field (MOSDEF; Kriek et al. 2015) survey. We also study the relations between dust in the CGM and the physical properties of the galaxies. This paper is structured as follows. The observations and data reduction are described in Section 2. We discuss the Ly α surface brightness profiles of the subsamples based on the spectral energy distribution (SED) fitting parameters in Section 3, and the reddening of Ly α photons in the CGM in Section 4. In Section 5, the relations between Ly α halo sizes and physical quantities are discussed. In addition, we discuss the implications of our results for the dust content in the CGM. Our results are summarized in Section 6. We use physical distances and assume a Λ CDM universe with $\Omega_m = 0.3$, $\Omega_{\Lambda} = 0.7$, and $H_0 = 70 \text{ km s}^{-1} \text{ Mpc}^{-1}$.

2. Observations and Data Reduction

2.1. MOSDEF Survey

Our sample was drawn from the MOSDEF survey (Kriek et al. 2015), which obtained rest-frame optical spectroscopy of \sim 1500 H-band selected star-forming galaxies and AGNs in the CANDELS fields (AEGIS, COSMOS, GOODS-N, GOODS-S, and UDS; Grogin et al. 2011; Koekemoer et al. 2011). The MOSDEF survey used the MOSFIRE spectrograph (McLean et al. 2012) on the Keck I telescope to obtain moderate-resolution ($R \sim 3000-3600$) rest-frame optical spectra ($\sim 3700-7000$ Å) at redshifts $1.4 \lesssim z \lesssim 3.8$. MOSDEF galaxies were selected based on preexisting photometric, grism, or spectroscopic redshifts where

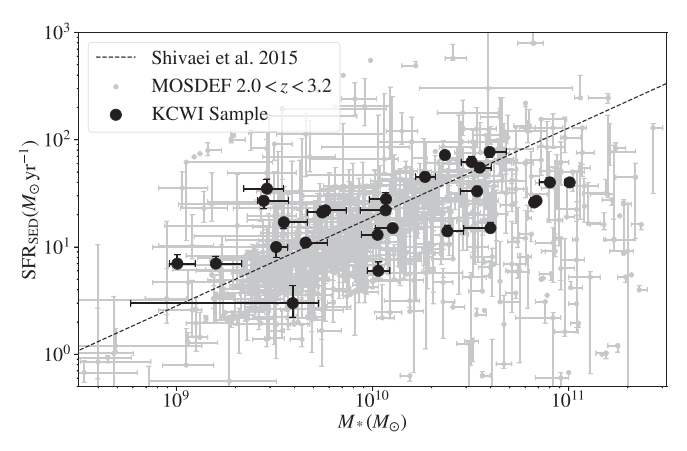


Figure 1. SFR vs. M_* for our KCWI sample (black) and MOSDEF galaxies (gray) with 2.0 < z < 3.2. Both SFR and M_* are derived through SED fitting, which is described in Section 2.6. The dashed line shows the best-fit linear relation between $\log({\rm SFR}/(M_\odot~{\rm yr}^{-1}))$ and $\log(M_*/M_\odot)$ found by Shivaei et al. (2015) for MOSDEF star-forming galaxies at z = 2.09 - 2.61.

the strong rest-frame optical lines fall in the YJHK atmospheric transmission windows (1.37 $\leq z \leq$ 1.70, 2.09 $\leq z \leq$ 2.61, or 2.95 $\leq z \leq$ 3.80). Details on the MOSDEF data reduction are provided in Kriek et al. (2015).

Emission lines were measured from the MOSDEF spectra using a Gaussian function and a linear continuum. The [O II] doublet was fitted with a double Gaussian function, and the $H\alpha$ and [N II] doublet was fit with three Gaussians. Line fluxes and errors were derived by perturbing the spectrum of each object by its error spectrum to generate 1000 realizations, measuring the line fluxes from each realization, and calculating the average line fluxes and dispersion. Systematic redshifts were derived using the strongest emission line. We refer the readers to Kriek et al. (2015) and Reddy et al. (2015) for further details on line flux measurements and slit loss corrections.

2.2. Sample Selection

Our sample contains 27 star-forming galaxies with redshifts 2.0 < z < 3.2 in the AEGIS, COSMOS, GOODS-N, and GOODS-S fields. We primarily focus on galaxies with detections of ${\rm H}\alpha$, ${\rm H}\beta$, and [O III], and either a detection or an upper limit on [N II]. These galaxies cover the full ranges of stellar mass and SFR for galaxies in the MOSDEF survey, as indicated in Figure 1.

2.3. KCWI Observations

The galaxies in our sample were observed over the course of eight nights in 2018–2020 using KCWI (Morrissey et al. 2018) on the Keck II telescope. The medium slicer and the BL grating with a central wavelength of 4500 Å were used, resulting in a 16.75×20.70 field of view and a spectral resolution of $R \sim 1800$. The typical integration time per pointing was ~ 5 hr and the average seeing was ~ 1.70 . The KCWI Data Reduction Pipeline was used to reduce individual cubes, and the various cubes constructed from exposures at different position angles were combined and drizzled onto a common grid (0.73×0.73) using custom-built Python software as described in Chen et al. (2021). Briefly, the reduction steps include overscan subtraction, cosmic-ray removal, scattered

https://github.com/Keck-DataReductionPipelines/KcwiDRP

light subtraction, wavelength calibration, flat-fielding, sky subtraction, cube generation, differential atmospheric refraction correction, and flux calibration. We also used median filtering to remove the low-frequency background structures. Finally, multiband images from the 3D-HST survey (described in Section 2.5) were stacked using inverse variance weighting, and this combined image was cross-correlated with the KCWI continuum image to calculate the alignment offset, which was used for the astrometric correction of the KCWI data. We refer readers to Chen et al. (2021) for more details.

2.4. 2D Lya Images

The 2D Ly α images of each galaxy were calculated from the 3D data cubes using a method similar to that described in Erb et al. (2018), briefly outlined as follows.

First, the fluxes in the central 9×9 pixels (2.7×2.7) of the reduced cubes were summed at each wavelength point to produce 1D spectra. For each wavelength point, the flux uncertainty was calculated by summing the uncertainty per pixel in quadrature. The continuum levels on the red and blue sides of the Ly α line, $c_{\text{red,spec}}$ and $c_{\text{blue,spec}}$, were calculated by averaging the spectrum in two windows spanning rest-frame wavelengths of 1269–1279 Å and 1160–1180 Å, respectively. The uncertainties of the red-side and blue-side continuum levels were calculated by summing the uncertainty of the 1D spectrum in quadrature within the two windows. The continuum level at Ly α , $c_{\text{Ly}\alpha,\text{spec}}$, was calculated as the average of the blue- and red-side continuum levels (Kornei et al. 2010), while its uncertainty was determined by summing the red-side and blue-side continuum uncertainties in quadrature.

Second, 2D images of Ly α ($I_{\rm Ly}\alpha$) and the red-side continuum ($I_{\rm cont,red}$) were extracted from the 3D data cube by collapsing the cube along the dispersion axis and summing over the wavelength regions 1210–1220 Å and 1269–1279 Å, respectively. The variance cube was summed along the dispersion axis within these two windows to obtain the 2D variance images. The square roots of the variance images were calculated as the uncertainty images.

Lastly, the continuum image underlying Ly α ($I_{\text{cont,Ly}\alpha}$) and the "Ly α -only" image ($I_{\text{Ly}\alpha,\text{only}}$) were calculated as follows:

$$I_{\text{cont,Ly}\alpha} = \frac{c_{\text{Ly}\alpha,\text{spec}}}{c_{\text{red,spec}}} \times I_{\text{cont,red}}$$
 (1)

$$I_{\text{Ly}\alpha,\text{only}} = I_{\text{Ly}\alpha} - I_{\text{cont,Ly}\alpha}.$$
 (2)

The uncertainties of these two images were calculated following a similar methodology to that described above.

2.5. 3D-HST Images

We used the publicly available multiband (F125W, F140W, F160W, F606W, and F814W) images that were compiled by the 3D-HST grism survey team (Grogin et al. 2011; Koekemoer et al. 2011; Skelton et al. 2014). The Hubble Space Telescope (HST) images were drizzled to a 0."06 pixel⁻¹ scale and point-spread function (PSF)-smoothed to the same 0."18 spatial resolution as the F160W data. We mosaicked the images from different filters using inverse variance weighting, and this combined image was used for the astrometric correction of the KCWI data and the calculation of the PSF of the KCWI observations.

2.6. Physical Properties

The SED parameters $(M_*, \text{SFR}, \text{age}, \text{and continuum reddening } E(B-V)_{\text{cont}})$ of the KCWI sample were derived using SED fitting as described in Reddy et al. (2015). We assumed constant star formation histories, the Bruzual & Charlot (2003) stellar population synthesis models at 0.2 Z_{\odot} , a Chabrier initial mass function (Chabrier 2003), and the SMC attenuation curve (Fitzpatrick & Massa 1990; Gordon et al. 2003). The SFR surface density ($\Sigma_{\rm SFR}$) and $\Sigma_{\rm SFR}$ normalized by stellar mass ($\Sigma_{\rm SSFR}$) were calculated as

$$\Sigma_{\rm SFR} = \frac{\rm SFR}{2\pi r_e^2} \tag{3}$$

$$\Sigma_{\rm sSFR} = \frac{\rm SFR}{2\pi r_e^2 M_*},\tag{4}$$

where SFR and M_* are the star formation rate and the stellar mass from SED fitting, and r_e is the effective radius from van der Wel et al. (2014), which contains half of the total HST/F160W light. In Figure 2 we show the histograms of physical quantities of the KCWI sample and the MOSDEF sample. The comparison shows that the KCWI sample is representative of the parent sample from which it was drawn.

3. Composite Images

3.1. Ly\alpha Surface Brightness Profiles and Scale Lengths

To examine how the halo properties vary with SED parameters, the galaxies were binned according to their SFR, M_* , age, $E(B-V)_{\rm cont}$, $\Sigma_{\rm SFR}$, and $\Sigma_{\rm sSFR}$. For each galaxy, a $9'' \times 9''$ image was extracted from its "Ly α -only" image. The unweighted average of these images was then used to create a composite image of each subsample. The uncertainty images were summed in quadrature to calculate the uncertainty of the composite image. The surface brightness profiles were calculated based on the stacked images in annuli with radii r=0''-4.''.5 and a width of 0.''.15. We used the Python package photutils to calculate the surface brightness flux density and its uncertainty.

The surface brightness profile of the Ly α halo is usually described by a decreasing exponential model (Steidel et al. 2011):

$$S(r) = C_n e^{-r/r_n}, (5)$$

where C_n is a constant and r_n is the scale length. However, since the profiles are not monotonically decreasing, we fit the surface brightness profiles with Equation (5) convolved with the seeing PSF at radii spanning from the radius at which Ly α peaks, out to 4."5. The seeing PSF for each subsample was calculated using the full width at half-maximum (FWHM) of Gaussian fits to the stacked HST and KCWI continuum images, i.e., FWHM_{PSF} = $\sqrt{\text{FWHM}_{KCWI}^2 - \text{FWHM}_{HST}^2}$. The average redshift of each subsample was then used to convert the scale length in angular size to physical distance. We note that the effect of the PSF is marginal since the Ly α emission is extended and the fitting range is large compared to the FWHM

These assumptions are based on previous work (Reddy et al. 2015, 2018; Shivaei et al. 2015; Weldon et al. 2022) that used MOSDEF galaxies.

https://photutils.readthedocs.io/en/stable/

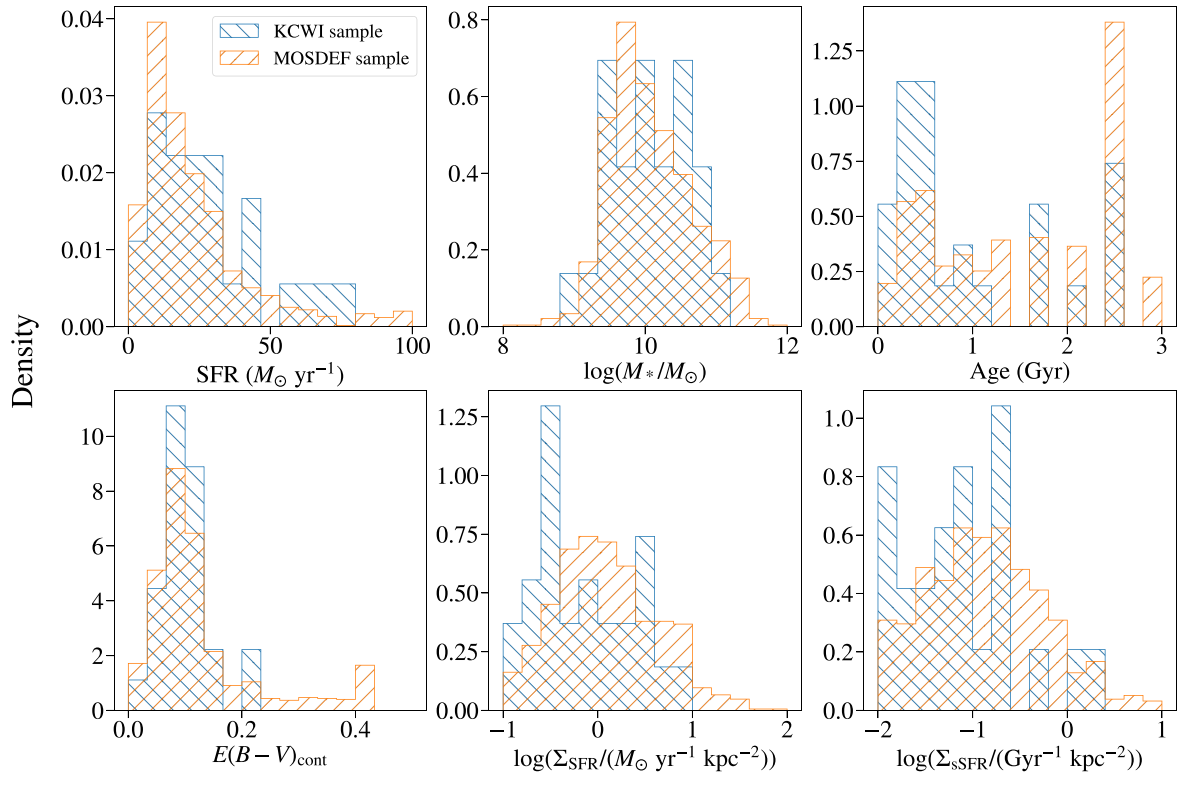


Figure 2. Density histograms of physical quantities of the KCWI sample and the MOSDEF galaxies at the same redshift (2.0 < z < 3.2).

of the PSF. The scale lengths r_n in proper kiloparsecs (pkpc) for the different subsamples are listed in Table 1.

Figures 3 and 4 show the composite profiles in two bins of SFR, stellar mass, age, $E(B-V)_{cont}$, Σ_{SFR} , and Σ_{sSFR} , respectively. The profiles have a nonmonotonic shape with a peak at $r \sim 1''$ for high SFR, low M_* , young ages, low reddening, and high $\Sigma_{\rm sSFR}$. On the other hand, the profiles for low SFR, high M_* , high reddening, old ages, and low $\Sigma_{\rm sSFR}$ exhibit a deficiency of Ly α within a \sim 0."7 radius. The former subsamples also have smaller scale lengths. For the SFR and stellar mass subsamples, the differences in the scale lengths between the low and high bins are $\sim 1.2\sigma$ and $\sim 2.5\sigma$, respectively, the latter being marginally significant. The differences in the scale lengths of the age, $E(B-V)_{cont}$, and $\Sigma_{\rm sSFR}$ subsamples are significant (>7 σ). Meanwhile, deficits of Ly α emission are indicated in both Σ_{SFR} subsamples, while the scale lengths of the halos are significantly different at the $>4\sigma$ level. The implications of these results are discussed in Section 5.2.

3.2. Down-the-barrel Ly\alpha Fractions

In Table 2, we present the down-the-barrel fractions (or upper limits) of Ly α emission. This quantity tells us the fraction of Ly α escaping along the same lines of sight that intersect with the nonresonant continuum emission. The down-the-barrel fraction $f_{\rm dtb}$ is calculated as

$$f_{\rm dtb} = L_{\rm Ly\alpha,c}/L_{\rm Ly\alpha,total},$$
 (6)

where $L_{\rm Ly\alpha,c}$ is the Ly α emission within an aperture of a diameter equal to the FWHM of the continuum emission, and $L_{\rm Ly\alpha,total}$ is the Ly α emission within the aperture that yields the highest signal-to-noise ratio (S/N) measurement of Ly α . All the fractions are less than 10%, indicating that the vast majority

Table 1 Scale Lengths r_n in Proper Kiloparsecs

Parameters	Threshold	Low Bin	High Bin
SFR	$22 M_{\odot} {\rm yr}^{-1}$	15.5 ± 3.7	10.9 ± 0.4
M_*	$10^{10.1}M_{\odot}$	10.6 ± 0.4	12.6 ± 0.7
Age	0.5 Gyr	8.8 ± 0.3	15.5 ± 0.9
$E(B-V)_{\rm cont}$	0.09	9.2 ± 0.4	21.6 ± 1.5
Σ_{SFR}	$0.78 M_{\odot} \mathrm{yr}^{-1} \mathrm{kpc}^{-2}$	21.9 ± 3.2	8.5 ± 0.5
$\Sigma_{\rm sSFR}$	$0.035 \; \mathrm{Gyr}^{-1} \; \mathrm{kpc}^{-2}$	17.4 ± 1.1	8.7 ± 0.4

of Ly α emission is resonantly scattered far from the continuum emission region. For all the SED properties examined here, the subsamples with larger scale lengths show absorption in their central regions and the differences in the down-the-barrel Ly α fraction between the subsamples are significant (>3 σ). These results are discussed in Section 5.1.

4. Dust Attenuation of Ly α

4.1. Ly\alpha Escape Fraction and Equivalent Width

A number of studies suggest that Lyman continuum (LyC) photons generally escape through the same low-column-density channels in the ISM as Ly α photons (Gnedin et al. 2008; Zackrisson et al. 2013; Trainor et al. 2015; Dijkstra et al. 2016; Ma et al. 2016, 2020; Reddy et al. 2016; Steidel et al. 2018; Kimm et al. 2019; Kakiichi & Gronke 2021). Thus studying the Ly α escape fraction is useful for understanding the escape of LyC photons, an important factor in cosmic reionization (Miralda-Escudé et al. 2000). Since Ly α photons can also resonantly scatter through the CGM and suffer preferential dust attenuation, the Ly α escape fraction can reveal information on dust in the CGM.

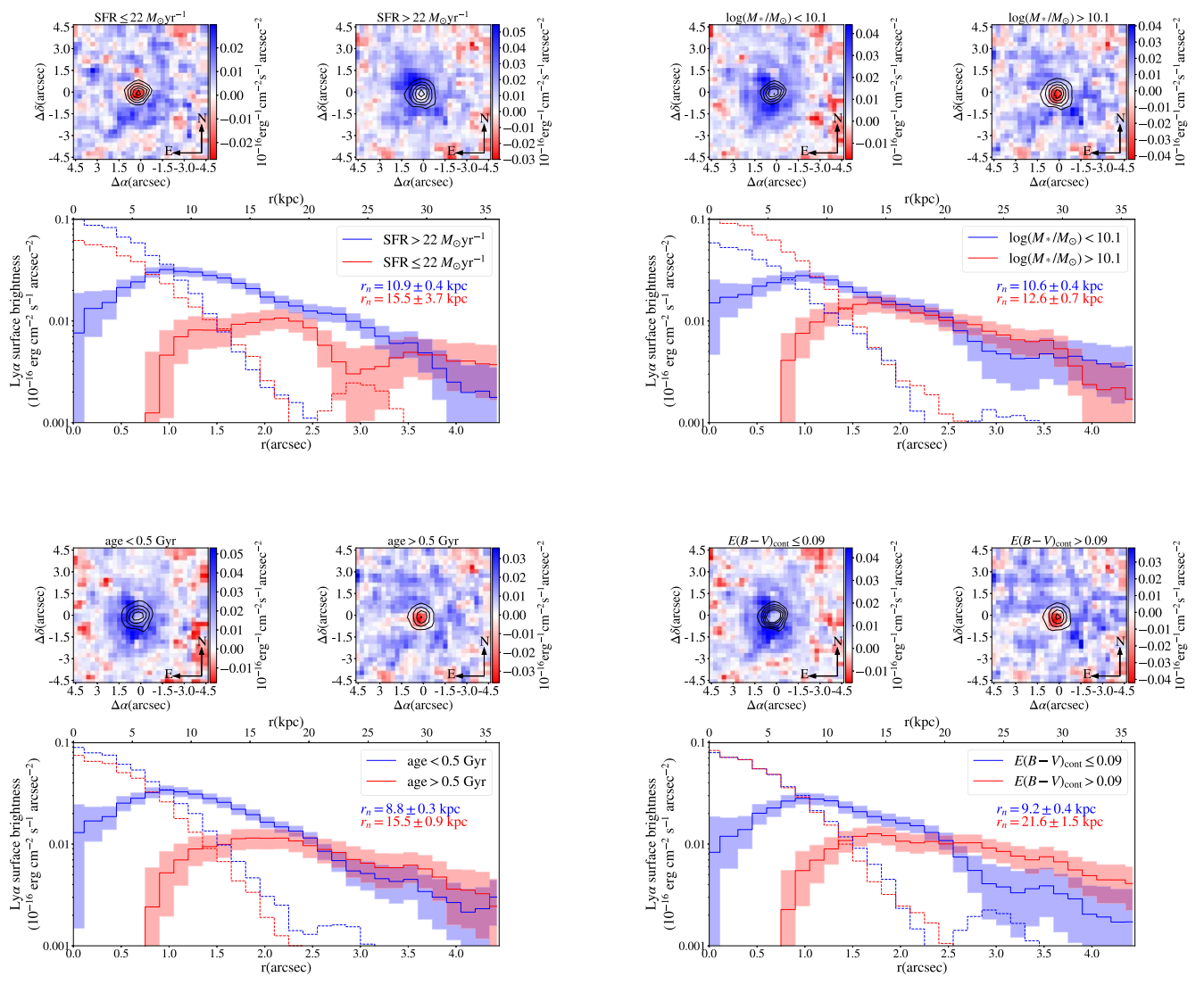


Figure 3. Top in each panel: composite Ly α images of SFR, M_* , age, and $E(B-V)_{\rm cont}$ subsamples. There is an even number of galaxies in each subsample. The black contours indicate the surface brightness of the composite continuum images, with the lowest level at 2.4×10^{-18} erg s⁻¹ cm⁻² arcsec⁻². Bottom in each panel: surface brightness profiles of composite Ly α images. The shaded regions indicate the 1σ error of the mean. The dashed lines indicate the surface brightness profiles of the continuum images. The straight lines indicate the best-fitting lines. The physical radius is calculated based on the average redshift of the sample (z = 2.41); r_n indicates the scale length of each subsample.

Here, we compute the effective attenuation of the Ly\$\alpha\$ line using the following procedure. Reddy et al. (2020) showed that the nebular dust attenuation curve derived for MOSDEF galaxies at $z\sim2$ is similar to the Galactic extinction curve (Cardelli et al. 1989). Using H\$\alpha\$ and H\$\beta\$ emission lines, corrected for Balmer absorption, we computed \$E(B-V)_{neb}\$ and the intrinsic (dust-corrected, assuming the Galactic extinction curve) H\$\alpha\$ luminosities. The Ly\$\alpha\$ (continuum) luminosities were calculated by finding the aperture that yields the highest S/N measurement of Ly\$\alpha\$ (continuum). A commonly used intrinsic flux ratio is \$F_{Ly\alpha}/F_{H\alpha} = 8.7\$ under the assumption of case B recombination and \$T_e = 10^4\$ K (Brocklehurst 1971). However, as shown by Reddy et al. (2022), an intrinsic flux ratio of 9.3 is more appropriate for galaxies in the MOSDEF survey, and thus we adopt this value. The Ly\$\alpha\$ escape fraction \$f_{\rm esc}\$ is defined as

$$f_{\rm esc} = \frac{L_{\rm Ly\alpha,obs}}{L_{\rm Ly\alpha,int}} = \frac{L_{\rm Ly\alpha,obs}}{9.3L_{\rm H\alpha,int}},$$
 (7)

where $L_{\text{Ly}\alpha,\text{obs}}$ and $L_{\text{Ly}\alpha,\text{int}}$ are the total observed and intrinsic $\text{Ly}\alpha$ luminosities, and $L_{\text{H}\alpha,\text{int}}$ is the intrinsic $\text{H}\alpha$ luminosity.

The Ly α escape fraction $f_{\rm esc}$ as a function of the rest-frame equivalent width $W_{\lambda}(Ly\alpha)$ (integrated over the entire Ly α halo) is presented in Figure 5. The rest-frame Ly α equivalent width was calculated using the observed Ly α and continuum luminosities. Note that for the following discussion, 11 galaxies that are close to the edge of the field of view or their neighbors are excluded since their Ly α luminosities could be underestimated due to the small field of view, or overestimated due to the contamination of their neighbors. A linear correlation is found between $f_{\rm esc}$ and $W_{\lambda}({\rm Ly}\alpha)$ with a Pearson correlation coefficient r = 0.57 and a probability of null correlation of p = 0.03. This is consistent with the result of Trainor et al. (2015) and Reddy et al. (2022), who found that $W_{\lambda}(Ly\alpha)$ correlates with $f_{\rm esc}$. Since the intrinsic Ly α luminosity $L(Ly\alpha)_{int}$ scales with the intrinsic $H\alpha$ luminosity $L(H\alpha)_{int}$, and $W_{\lambda}(Ly\alpha)$ is proportional to the ratio of the observed Ly α

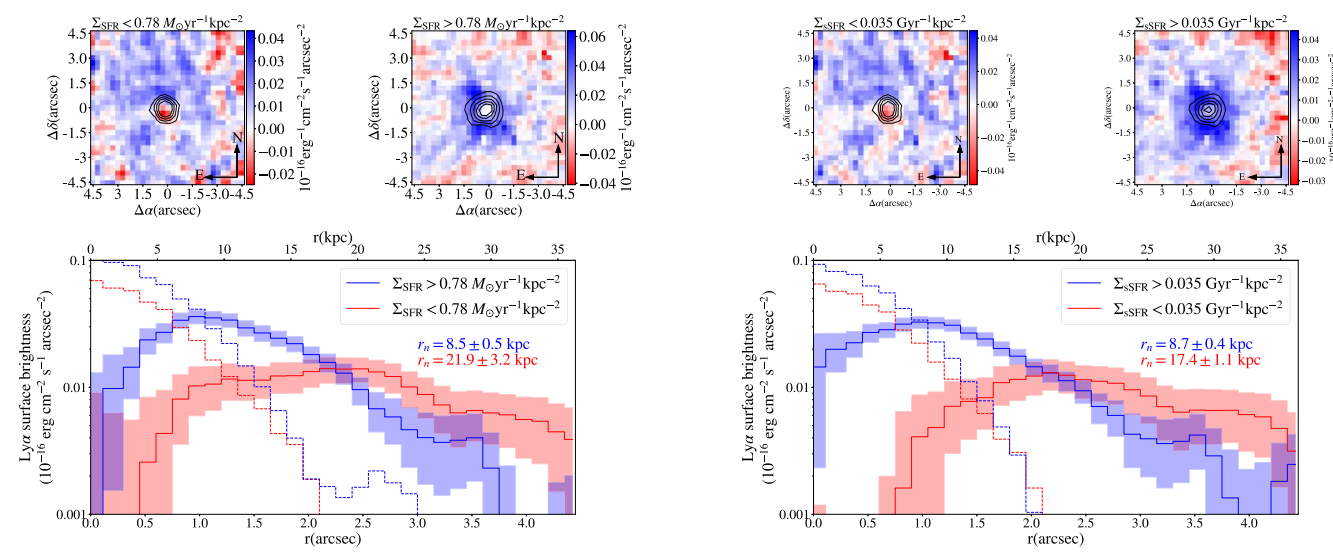


Figure 4. Same as Figure 3 but for the Σ_{SFR} and Σ_{sSFR} subsamples.

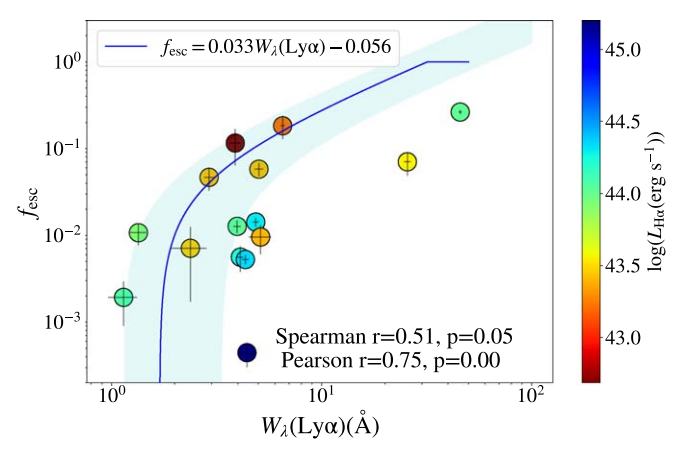


Figure 5. Ly α escape fraction vs. Ly α equivalent width in rest frame. The shaded region indicates the 1σ confidence interval. The data points are colored by their H α luminosities.

Parameters	Threshold	Low Bin	High Bin
SFR	$22 M_{\odot} \mathrm{yr}^{-1}$	< 0.05	0.06 ± 0.01
M_*	$10^{10.1}M_{\odot}$	0.09 ± 0.01	< 0.03
Age	0.5 Gyr	0.09 ± 0.01	< 0.03
$E(B-V)_{\rm cont}$	0.09	0.08 ± 0.01	< 0.03
$\Sigma_{ m SFR}$	$0.78 M_{\odot} \mathrm{yr}^{-1} \mathrm{kpc}^{-2}$	0.01 ± 0.01	0.10 ± 0.01
$\Sigma_{\rm sSFR}$	$0.035 \mathrm{Gyr}^{-1} \mathrm{kpc}^{-2}$	< 0.024	0.10 ± 0.01

luminosity to the observed UV luminosity $L(UV)_{obs}$,

$$\frac{f_{\rm esc}}{W_{\lambda}({\rm Ly}\alpha)} \propto \frac{L({\rm UV})_{\rm obs}}{L({\rm H}\alpha)_{\rm int}} = \frac{L({\rm UV})_{\rm int}}{L({\rm H}\alpha)_{\rm int}} \times 10^{-0.4k({\rm UV})E(B-V)}. \tag{8}$$

The scatter in the linear relation between $f_{\rm esc}$ and $W_{\lambda}({\rm Ly}\alpha)$ stems from differences in E(B-V) and the variation in the H α -to-UV ratio. For galaxies with higher attenuation, $W_{\lambda}({\rm Ly}\alpha)$ would be larger relative to $f_{\rm esc}$. On the other hand, Fetherolf et al. (2021) and Rezaee et al. (2023) found that galaxies with higher H α

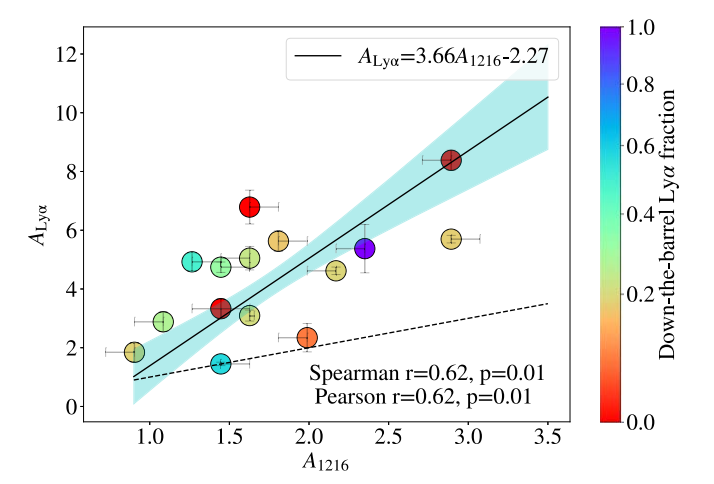


Figure 6. $A_{\rm Ly\alpha}$ as a function of A_{1216} . The solid line indicates the best-fitting line while the dashed line indicates the identity line. The shaded region indicates the 1σ confidence interval. The data points are colored by their down-the-barrel ${\rm Ly}\alpha$ fraction.

luminosities (higher instantaneous SFR) have higher H α -to-UV ratios. In Figure 5, galaxies with relatively lower $f_{\rm esc}$ have larger H α luminosities, and hence have lower $f_{\rm esc}/W_{\lambda}({\rm Ly}\alpha)$.

Due to their resonant scattering, $\text{Ly}\alpha$ photons are more likely to be destroyed by dust grains in the CGM relative to the nonresonant UV continuum photons. We can test for this effect using our data. Figure 6 shows the attenuation of $\text{Ly}\alpha$ ($A_{\text{Ly}\alpha}$) versus the attenuation of continuum flux at 1216 Å (A_{1216}). The attenuation of $\text{Ly}\alpha$ photons can be derived from the $\text{Ly}\alpha$ escape fraction, i.e., $A_{\text{Ly}\alpha} = -2.5 \log(f_{\text{esc}})$. The attenuation of continuum flux at 1216 Å was calculated using the SMC attenuation curve and $E(B-V)_{\text{cont}}$. The data points are color coded by the down-the-barrel $\text{Ly}\alpha$ fraction (the ratio of $\text{Ly}\alpha$ flux spatially coincident with the continuum to the total $\text{Ly}\alpha$ flux). $A_{\text{Ly}\alpha}$ is found to be positively correlated with A_{1216} and $A_{\text{Ly}\alpha}$ is greater than A_{1216} for dustier galaxies. This result shows that the resonant scattering of $\text{Ly}\alpha$ results in a higher

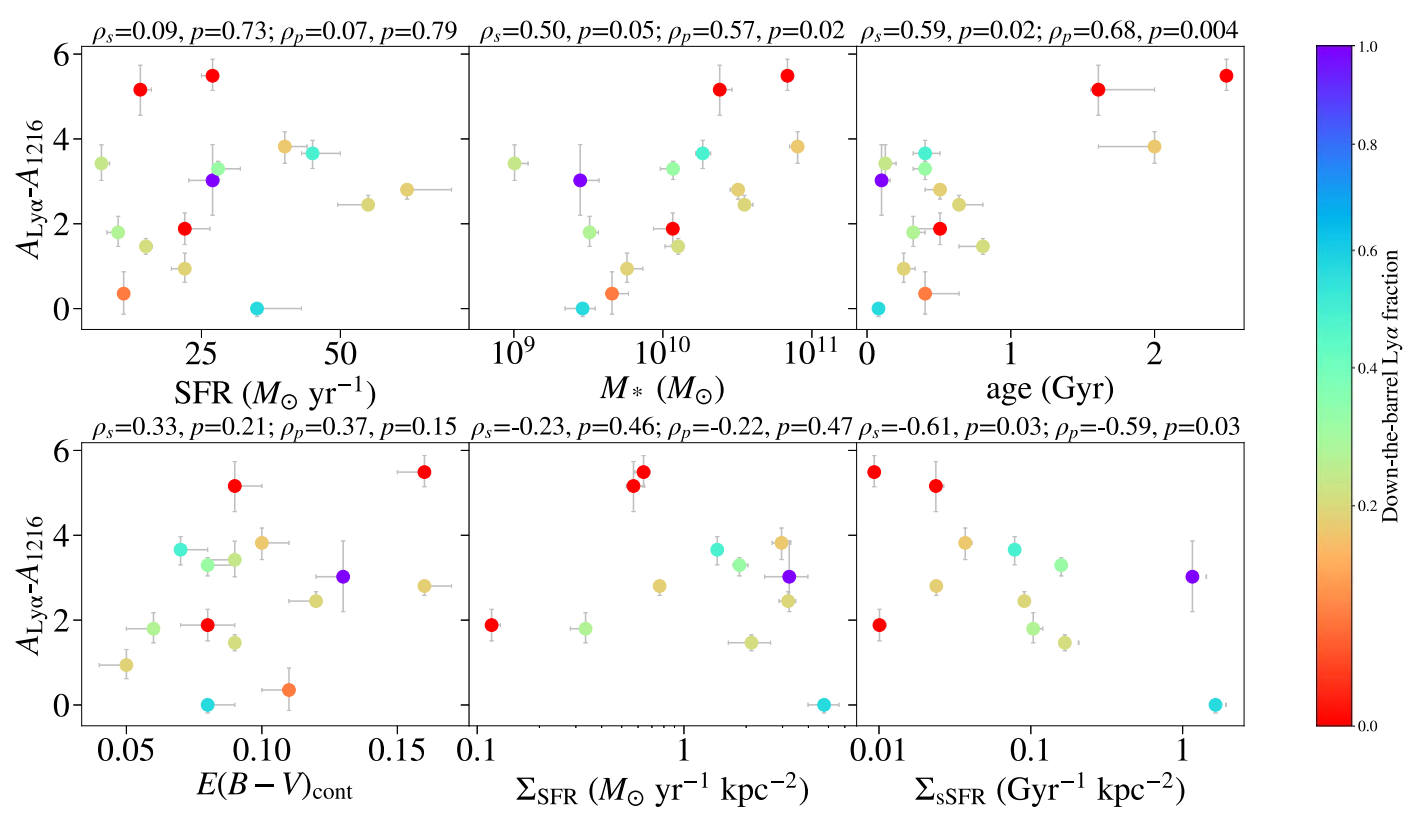


Figure 7. $A_{\text{Ly}\alpha} - A_{1216}$ as a function of different physical properties. Spearman and Pearson correlation coefficients and their *p*-values are shown at the top of each grid. The data points are colored by their down-the-barrel Ly α fraction. The only significant correlations are with M_* , age, and Σ_{SSFR} .

effective attenuation of Ly α photons relative to the nonresonant UV continuum photons.

The enhancement of attenuation for Ly α , $\Delta A = A_{\rm Ly}\alpha - A_{1216}$, as a function of different physical properties is shown in Figure 7. The difference in attenuation is correlated with stellar mass and age, but anticorrelated with $\Sigma_{\rm sSFR}$. A weak correlation is found for $E(B-V)_{\rm cont}$. No correlation is found for SFR and $\Sigma_{\rm SFR}$. The implications of these results are discussed in Section 5.3.

5. Discussion

In this section, we discuss how the down-the-barrel $Ly\alpha$ fraction (Section 5.1), the scale lengths of the $Ly\alpha$ halos (Section 5.2), and dust in the CGM depend on the physical properties of the host galaxies (Section 5.3). These relations are important for understanding the escape of $Ly\alpha$ photons and the properties of the CGM.

5.1. Down-the-barrel Ly\alpha Fraction

There are two ways for $\mathrm{Ly}\alpha$ photons to escape from the CGM of a galaxy: one is to escape after multiple resonant scatterings (Laursen & Sommer-Larsen 2007); the other is to escape through the low-column-density channels that are created by strong stellar winds from massive stars and/or supernovae (Gnedin et al. 2008; Zackrisson et al. 2013; Ma et al. 2016; Sharma et al. 2017). The latter is also thought to be a mechanism through which LyC photons escape (Gnedin et al. 2008; Ma et al. 2016, 2020; Kimm et al. 2019; Kakiichi & Gronke 2021). Thus the dependence of down-the-barrel $\mathrm{Ly}\alpha$ fractions (f_{dtb}) on physical properties can reveal how these low-column-density channels are regulated.

In Table 2, we list the down-the-barrel Ly α fractions of different subsamples. Upper limits of f_{dtb} are obtained for galaxies with lower SFR and $\Sigma_{\rm sSFR}$, larger stellar mass and $E(B-V)_{cont}$, and older ages. A deficit of Ly α is also observed in the center of stacked images of low- Σ_{SFR} galaxies (Figures 3 and 4). A deficit of Ly α is also observed for the "Ly α Abs" sample (i.e., those galaxies with the down-the-barrel Ly α in net absorption) of Steidel et al. (2011) and in the non-Ly α emitter realizations of Momose et al. (2014, 2016). On the other hand, the Ly α surface brightness profiles of the remaining subsamples are suppressed in the central regions. This effect has also been reproduced by the simulation of Laursen et al. (2009), in which they found that this suppression is caused by the inclusion of dust. Equation (2) of Steidel et al. (2011) provided a model that explains the deficit and suppression of Ly α : Ly α photons created in the central region are destroyed or scattered to outer regions because of the high covering fraction of neutral gas at small impact parameters and near the systemic redshift of the galaxy.

We find that galaxies with higher SFRs also have higher $f_{\rm dtb}$. This is consistent with a scenario in which low-column-density channels are caused by stellar feedback, which is prevalent in galaxies with higher SFRs. However, the difference between the $f_{\rm dtb}$ of the high-SFR subsample and the upper limit of the $f_{\rm dtb}$ of the low-SFR subsample is $\sim 1\sigma$. This insignificant difference may be due to the fact that galaxies with higher SFRs are also more gas-rich (and dust-rich) (Reddy et al. 2010, 2015; Domínguez et al. 2013; Sanders et al. 2023), such that it may be more difficult for stellar feedback to puncture channels through the ISM/CGM of these galaxies. Furthermore, high-SFR galaxies are generally more massive (Figure 1), and in the following analysis, we will show that

the high gravitational potential associated with high-stellarmass galaxies can impede the creation of low-column-density channels. Thus SFR alone may not be a good indicator of $f_{\rm dtb}$ and hence LyC escape.

A commonly used indicator of LyC escape is Σ_{SFR} (Alexandroff et al. 2015; Sharma et al. 2016; Naidu et al. 2020; Flury et al. 2022), as it is a proxy of star formation feedback and potentially the creation of low-column-density channels (Heckman et al. 2001). A significant difference in $f_{\rm dtb}$ is found between high- and low- $\Sigma_{\rm SFR}$ galaxies, which is expected since high- $\Sigma_{\rm SFR}$ galaxies are believed to be quite efficient at creating low-column-density channels in the ISM (Sharma et al. 2016, 2017; Verhamme et al. 2017; Cen 2020; Naidu et al. 2020). Yet there may be other factors that influence the down-the-barrel fraction of Ly α . In particular, Reddy et al. (2022) highlight the potential importance of gravitational potential in influencing the porosity of the ISM and the leakage of Ly α and LyC photons. Stellar mass is a rough proxy for dynamical mass or gravitational potential (Price et al. 2020) and we do find that more massive galaxies exhibit lower f_{dtb} , suggesting that the gravitational potential may play a role in regulating the escape of Ly α . Therefore we examined $\Sigma_{\rm SFR}/M_*$ to ascertain whether galaxies at a fixed $\Sigma_{\rm SFR}$ but lower M_* have a larger down-the-barrel Ly α escape fraction. We find that the high- $\Sigma_{\rm sSFR}$ bin has a larger down-the-barrel fraction than the low- $\Sigma_{\rm sSFR}$ bin. When binned solely by $\Sigma_{\rm SFR}$, the difference in f_{dtb} between subsamples is smaller than when binned by $\Sigma_{\rm sSFR}$. Therefore, galaxies with high and low $f_{\rm dtb}$ can be more effectively separated by $\Sigma_{\rm sSFR}$ (Figure 7). This suggests that gravitational potential may be an important factor in the porosity of the ISM and the leakage of Ly α photons, consistent with the analysis of Reddy et al. (2022).

We also examine the dependence of $f_{\rm dtb}$ on reddening, finding that galaxies with lower $E(B-V)_{\rm cont}$ show higher $f_{\rm dtb}$. This result is consistent with Reddy et al. (2016), who found that dustier galaxies have larger neutral gas covering fractions. We also find that $f_{\rm dtb}$ anticorrelates with the age of galaxies, which is expected given that young galaxies are less massive and less dusty.

5.2. Scale Lengths of Ly\alpha Halos

The sizes of Ly α halos are typically parameterized by their exponential scale lengths. The relations between the scale lengths and other physical quantities are of interest since they reveal the amount and distribution of gas and dust in the CGM. In Table 1, we report the scale lengths of the profiles of the various subsamples, which are found to vary from \sim 8 to 25 pkpc. These results are consistent with both Steidel et al. (2011; UV continuum selected galaxies; \sim 25 pkpc) and Momose et al. (2016; Ly α emitters (LAEs); \sim 10 pkpc), and are slightly larger than the scale lengths found by Xue et al. (2017; UV continuum faint LAEs; ~6 pkpc). The sample used in Xue et al. (2017) contains galaxies with $z \sim 3.78$, whose UV continuum sizes are smaller than those in our sample. Given the relation between Ly α halo scale length and UV continuum scale length (Wisotzki et al. 2016; Leclercq et al. 2017), it is reasonable to expect that our KCWI sample has longer Ly α scale lengths than the sample used in Xue et al. (2017).

Comparing Tables 1 and 2, we find that subsamples with higher $f_{\rm dtb}$ have shorter scale lengths. This relation indicates that the number of low-column-density channels might regulate the scale length of Ly α halos. A natural explanation is that with

more low-column-density channels, the fraction of Ly α photons that are scattered into the CGM is lower. This effect would enhance the Ly α surface brightness profile in the inner region and reduce it in the outer region, thus resulting in a shorter scale length for the extended Ly α emission.

For our subsamples, the scale lengths of high-SFR galaxies are found to be slightly smaller ($\sim 1\sigma$) than those of low-SFR galaxies. Wisotzki et al. (2016) and Leclercq et al. (2017) also found that for LAEs, $M_{\rm UV}$, which is an indicator of SFR, is correlated with the scale length. However, in another study of LAEs, Matsuda et al. (2012) found no correlation between scale length and central (within 1") UV luminosity. Moreover, Feldmeier et al. (2013) showed that UV-bright galaxies have slightly larger Ly α halos. These mixed results could arise from the fact that star-forming galaxies are also gas- and dust-rich, so there may not be a direct correlation between SFR and the scale length in the same way that we found no correlation between SFR and $f_{\rm dtb}$ (Section 3.2).

Table 1 indicates that scale lengths increase with reddening (or dustiness). This result would be expected if galaxies with more dust contain more gas and therefore have higher gas covering fractions (Reddy et al. 2016). In this case, a larger fraction of $\text{Ly}\alpha$ photons scatter away from the continuum regions and either escape or are destroyed by dust at larger radii. The resonant scattering would flatten the $\text{Ly}\alpha$ surface brightness profile, resulting in a longer scale length.

High-mass galaxies in the KCWI sample are found to have slightly larger Ly α halos likely because they have higher SFRs and are dustier. In Section 5.1 we also show that massive galaxies have stronger gravitational potential, which impedes the creation of low-column-density channels. Reddy et al. (2022) also found that the Ly α equivalent width anticorrelates with stellar mass, suggesting lower gas covering fractions in less massive galaxies. Combining the effect of stellar mass and dustiness, it is not surprising that younger galaxies have shorter scale lengths given that they are less dusty and less massive. We also find that the younger galaxies have higher $\Sigma_{\rm sSFR}$ (Pearson r = -0.772, p-value <0.001), and hence have a larger fraction of Ly α emission coming from the continuum region, and a smaller fraction that is resonantly scattered to large radii. Thus, these younger galaxies have shorter halo scale lengths.

Unlike that of SFR, the impact of SFR surface density on the scale length is significant. The high- $\Sigma_{\rm SFR}$ subsample exhibits the smallest scale length (<10 pkpc) of any of the subsamples while the scale length of the low- $\Sigma_{\rm SFR}$ subsample is the largest among all the subsamples. Galaxies with higher $\Sigma_{\rm SFR}$ are more compact, and thus their gas distribution may also be more compact. Their Ly α surface brightness profiles are then expected to be decreasing steeply. In Section 5.1 we discussed that high $\Sigma_{\rm SSFR}$ plays an important role in creating low-column-density channels in the ISM. Those channels would ease the escape of Ly α photons at a smaller radius and therefore result in a smaller scale length.

5.3. Dust in the CGM

Due to their resonant nature, Ly α photons may suffer varying degrees of attenuation relative to the stellar continuum. In particular, a larger number of resonant scatterings in a dusty medium results in a higher probability for Ly α photons to be absorbed by dust, resulting in an increase in the attenuation of Ly α . On the other hand, Ly α photons exiting down the barrel of the galaxy are likely undergoing fewer resonant scatterings

and escaping the ISM through channels of low gas and dust column densities. In this case, these $Ly\alpha$ photons may not suffer much attenuation (e.g., Trainor et al. 2015; Reddy et al. 2022). Scarlata et al. (2009) showed that observed high $Ly\alpha/H\alpha$ and $H\alpha/H\beta$ line ratios can be reproduced by a clumpy dust distribution, implying the existence of low-column-density sightlines. To study the dust content of the CGM, we focus on the attenuation of $Ly\alpha$ photons that escape from the halo. When assuming that all the down-the-barrel emission comes from the low-column-density sightlines and is not significantly attenuated, the escape fraction of the halo $Ly\alpha$ photons can be defined as

$$f_{\text{halo}} = (L_{\text{obs}} - L_{\text{dtb}})/(L_{\text{int}} - L_{\text{dtb}}), \tag{9}$$

where $L_{\rm obs}$, $L_{\rm dtb}$, and $L_{\rm int}$ represent the total observed, down-the-barrel, and intrinsic Ly α luminosity, respectively. Because most of the Ly α emission comes from the halo (>90%), $L_{\rm dtb}$ is typically much smaller than $L_{\rm obs}$ and $L_{\rm int}$. Therefore, we can make the approximation that

$$f_{\rm halo} \approx L_{\rm obs}/L_{\rm int} = f_{\rm esc}.$$
 (10)

Since $f_{\rm esc}=10^{-0.4A_{{\rm Ly}\alpha}},~A_{{\rm Ly}\alpha}$ can be used to describe the attenuation of halo ${\rm Ly}\alpha$ photons.

Reddy et al. (2016) found that galaxies with higher E(B-V) have a larger covering fraction of optically thick H I gas and therefore a larger effective attenuation for Ly α . It would also not be unreasonable to expect that more reddened galaxies also have more dust in their CGM. This could explain why ΔA correlates with stellar mass and age, since massive and older galaxies have higher E(B-V). However, we only find a marginal correlation between $E(B-V)_{\rm cont}$ and ΔA . The marginal correlation may arise from the fact that stellar feedback would expel dust into the CGM and therefore reduce $E(B-V)_{\rm cont}$. As a result, galaxies with low $E(B-V)_{\rm cont}$ may also have substantial dust in their CGM.

In our sample, we find no relation between $E(B-V)_{\rm cont}$ and $\Sigma_{\rm sSFR}$, indicating that higher- $\Sigma_{\rm sSFR}$ galaxies may not have more dust in their CGM. Given that no relation is found between $\Sigma_{\rm SFR}$ and ΔA , we conclude that the anticorrelation between $\Sigma_{\rm SFR}$ and ΔA is due to the relation between stellar mass and ΔA .

6. Summary

In this paper, we utilize KCWI to observe the $Ly\alpha$ halos of 27 galaxies with spectroscopic redshifts. We study the relations between halo properties and physical quantities. The dust content in the CGM is also discussed. The major results of our paper are summarized as follows:

- 1. We find extended Ly α halos in the stacks of all subsamples (Figures 3 and 4). A deficit of Ly α is detected in the center of galaxies with lower SFR and $\Sigma_{\rm sSFR}$, higher stellar masses, older ages, and higher $E(B-V)_{\rm cont}$. Both $\Sigma_{\rm SFR}$ subsamples show a deficit of Ly α in their center. For the rest of the subsamples, the Ly α surface brightness densities are suppressed in the central region, which has not been seen in past studies of LAEs.
- 2. We investigate the down-the-barrel Ly α fraction and the scale length of Ly α halos as a function of various physical quantities (Tables 1 and 2). The down-the-barrel Ly α fraction correlates with SFR, $\Sigma_{\rm SFR}$, and $\Sigma_{\rm sSFR}$, and anticorrelates with stellar mass, age, and $E(B-V)_{\rm cont}$. On the other hand, scale

length correlates with stellar mass, age, and $E(B-V)_{\rm cont}$, and anticorrelates with SFR, $\Sigma_{\rm SFR}$, and $\Sigma_{\rm sSFR}$.

3. The effective attenuation of Ly α is higher than the attenuation of UV continuum photons at the same wavelength (Figure 6). The enhancement of attenuation correlates with stellar mass, age, and $E(B-V)_{\rm cont}$ and anticorrelates with $\Sigma_{\rm sSFR}$. No correlation is found for SFR and $\Sigma_{\rm SFR}$ (Figure 7).

In this paper, we show that $Ly\alpha$ halo properties are regulated by the neutral gas covering fraction (which is indicated by the $Ly\alpha$ down-the-barrel fraction). This covering fraction is affected by factors such as the amount of gas and dust, and stellar feedback. We also investigate the role of gravitational potential in affecting the intensity of stellar feedback and regulating the $Ly\alpha$ halo properties. In addition, by examining the enhancement of $Ly\alpha$ attenuation, we find that more reddened galaxies have more dust in their CGM.

In this paper, we present an analysis of the variation in $Ly\alpha$ halo profiles with commonly determined physical properties of galaxies, including stellar mass, SFR, reddening, and SFR surface density. There are other properties of galaxies that are believed to correlate with $Ly\alpha$ (and LyC) escape, including the [OIII]/[OII] ratio and interstellar absorption line equivalent widths. A future study will focus on these additional properties to shed further light on the mechanisms for $Ly\alpha$ and LyC escape.

Acknowledgments

We acknowledge support from NSF AAG grants AST1312780, 1312547, 1312764, and 1313171, grant AR13907 from the Space Telescope Science Institute, and grant NNX16AF54G from the NASA ADAP program. We thank the 3D-HST Collaboration, which provided the spectroscopic and photometric catalogs used to select the MOSDEF targets and derive stellar population parameters. This research made use of Astropy, 10 a community-developed core Python package for astronomy (Astropy Collaboration et al. 2013, 2018, 2022). The authors wish to recognize and acknowledge the very significant cultural role and reverence that the summit of Maunakea has always had within the indigenous Hawaiian community. We are most fortunate to have the opportunity to conduct observations from this mountain. This research made use of Photutils, an Astropy package for detection and photometry of astronomical sources (Bradley et al. 2023).

References

Adelberger, K. L., Steidel, C. C., Kollmeier, J. A., & Reddy, N. A. 2006, ApJ, 637, 74

Alexandroff, R. M., Heckman, T. M., Borthakur, S., Overzier, R., & Leitherer, C. 2015, ApJ, 810, 104

Astropy Collaboration, Price-Whelan, A. M., Lim, P. L., et al. 2022, ApJ, 935, 167

Astropy Collaboration, Price-Whelan, A. M., Sipőcz, B. M., et al. 2018, AJ, 156, 123

Astropy Collaboration, Robitaille, T. P., Tollerud, E. J., et al. 2013, A&A, 558, A33

Bacon, R., Accardo, M., Adjali, L., et al. 2010, Proc. SPIE, 7735, 773508 Borthakur, S., Heckman, T. M., Leitherer, C., & Overzier, R. A. 2014, Sci, 346, 216

Bradley, L., Sipőcz, B., Robitaille, T., et al. 2023, astropy/photutils: 1.8.0, v1.8.0, Zenodo, doi:10.5281/zenodo.7946442

Brocklehurst, M. 1971, MNRAS, 153, 471

https://www.astropy.org/

```
Bruzual, G., & Charlot, S. 2003, MNRAS, 344, 1000
Byrohl, C., Nelson, D., Behrens, C., et al. 2021, MNRAS, 506, 5129
Cardelli, J. A., Clayton, G. C., & Mathis, J. S. 1989, ApJ, 345, 245
Cen, R. 2020, ApJL, 889, L22
Chabrier, G. 2003, PASP, 115, 763
Chen, Y., Steidel, C. C., Erb, D. K., et al. 2021, MNRAS, 508, 19
Dijkstra, M., Gronke, M., & Venkatesan, A. 2016, ApJ, 828, 71
Dijkstra, M., Haiman, Z., & Spaans, M. 2006, ApJ, 649, 14
Dijkstra, M., & Kramer, R. 2012, MNRAS, 424, 1672
Dijkstra, M., & Loeb, A. 2009, MNRAS, 400, 1109
Domínguez, A., Siana, B., Henry, A. L., et al. 2013, ApJ, 763, 145
Erb, D. K., Li, Z., Steidel, C. C., et al. 2023, ApJ, 953, 118
Erb, D. K., Steidel, C. C., & Chen, Y. 2018, ApJL, 862, L10
Faucher-Giguère, C.-A., Kereš, D., Dijkstra, M., Hernquist, L., &
   Zaldarriaga, M. 2010, ApJ, 725, 633
Feldmeier, J. J., Hagen, A., Ciardullo, R., et al. 2013, ApJ, 776, 75
Fetherolf, T., Reddy, N. A., Shapley, A. E., et al. 2021, MNRAS, 508, 1431
Fitzpatrick, E. L., & Massa, D. 1990, ApJS, 72, 163
Flury, S. R., Jaskot, A. E., Ferguson, H. C., et al. 2022, ApJ, 930, 126
Gnedin, N. Y., Kravtsov, A. V., & Chen, H.-W. 2008, ApJ, 672, 765
Goerdt, T., Dekel, A., Sternberg, A., et al. 2010, MNRAS, 407, 613
Gordon, K. D., Clayton, G. C., Misselt, K. A., Landolt, A. U., & Wolff, M. J.
  2003, ApJ, 594, 279
Grogin, N. A., Kocevski, D. D., Faber, S. M., et al. 2011, ApJS, 197, 35
Hayes, M., Schaerer, D., Östlin, G., et al. 2011, ApJ, 730, 8
Heckman, T. M., Sembach, K. R., Meurer, G. R., et al. 2001, ApJ, 558, 56
Jaskot, A. E., Dowd, T., Oey, M. S., Scarlata, C., & McKinney, J. 2019, ApJ,
   885, 96
Kakiichi, K., & Gronke, M. 2021, ApJ, 908, 30
Kikuta, S., Matsuda, Y., Inoue, S., et al. 2023, ApJ, 947, 75
Kimm, T., Blaizot, J., Garel, T., et al. 2019, MNRAS, 486, 2215
Koekemoer, A. M., Faber, S. M., Ferguson, H. C., et al. 2011, ApJS, 197, 36
Kornei, K. A., Shapley, A. E., Erb, D. K., et al. 2010, ApJ, 711, 693
Kriek, M., Shapley, A. E., Reddy, N. A., et al. 2015, ApJS, 218, 15
Lake, E., Zheng, Z., Cen, R., et al. 2015, ApJ, 806, 46
Laursen, P., & Sommer-Larsen, J. 2007, ApJL, 657, L69
Laursen, P., Sommer-Larsen, J., & Andersen, A. C. 2009, ApJ, 704, 1640
Leclercq, F., Bacon, R., Wisotzki, L., et al. 2017, A&A, 608, A8
Ma, X., Hopkins, P. F., Kasen, D., et al. 2016, MNRAS, 459, 3614
Ma, X., Quataert, E., Wetzel, A., et al. 2020, MNRAS, 498, 2001
Martin, C., Moore, A., Morrissey, P., et al. 2010, Proc. SPIE, 7735, 77350M
```

Mas-Ribas, L., & Dijkstra, M. 2016, ApJ, 822, 84

```
Matsuda, Y., Yamada, T., Hayashino, T., et al. 2012, MNRAS, 425, 878
McLean, I. S., Steidel, C. C., Epps, H. W., et al. 2012, Proc. SPIE, 8446,
  84460I
Meier, D. L., & Terlevich, R. 1981, ApJL, 246, L109
Miralda-Escudé, J., Haehnelt, M., & Rees, M. J. 2000, ApJ, 530, 1
Momose, R., Ouchi, M., Nakajima, K., et al. 2014, MNRAS, 442, 110
Momose, R., Ouchi, M., Nakajima, K., et al. 2016, MNRAS, 457, 2318
Morrissey, P., Matuszewski, M., Martin, C., et al. 2012, Proc. SPIE, 8446,
Morrissey, P., Matuszewski, M., Martin, D. C., et al. 2018, ApJ, 864, 93
Naidu, R. P., Tacchella, S., Mason, C. A., et al. 2020, ApJ, 892, 109
Orsi, A., Lacey, C. G., & Baugh, C. M. 2012, MNRAS, 425, 87
Price, S. H., Kriek, M., Barro, G., et al. 2020, ApJ, 894, 91
Reddy, N. A., Erb, D. K., Pettini, M., Steidel, C. C., & Shapley, A. E. 2010,
    nJ. 712, 1070
Reddy, N. A., Kriek, M., Shapley, A. E., et al. 2015, ApJ, 806, 259
Reddy, N. A., Oesch, P. A., Bouwens, R. J., et al. 2018, ApJ, 853, 56
Reddy, N. A., Shapley, A. E., Kriek, M., et al. 2020, ApJ, 902, 123
Reddy, N. A., Steidel, C. C., Pettini, M., Bogosavljević, M., & Shapley, A. E.
  2016, ApJ, 828, 108
Reddy, N. A., Topping, M. W., Shapley, A. E., et al. 2022, ApJ, 926, 31
Rezaee, S., Reddy, N. A., Topping, M. W., et al. 2023, MNRAS, 526, 1512
Rivera-Thorsen, T. E., Hayes, M., Östlin, G., et al. 2015, ApJ, 805, 14
Rosdahl, J., & Blaizot, J. 2012, MNRAS, 423, 344
Sanders, R. L., Shapley, A. E., Jones, T., et al. 2023, ApJ, 942, 24
Scarlata, C., Colbert, J., Teplitz, H. I., et al. 2009, ApJL, 704, L98
Sharma, M., Theuns, T., Frenk, C., et al. 2016, MNRAS, 458, L94
Sharma, M., Theuns, T., Frenk, C., et al. 2017, MNRAS, 468, 2176
Shivaei, I., Reddy, N. A., Shapley, A. E., et al. 2015, ApJ, 815, 98
Skelton, R. E., Whitaker, K. E., Momcheva, I. G., et al. 2014, ApJS, 214, 24
Steidel, C. C., Bogosavljević, M., Shapley, A. E., et al. 2011, ApJ, 736, 160
Steidel, C. C., Bogosavljević, M., Shapley, A. E., et al. 2018, ApJ, 869, 123
Trainor, R. F., Steidel, C. C., Strom, A. L., & Rudie, G. C. 2015, ApJ, 809, 89
van der Wel, A., Franx, M., van Dokkum, P. G., et al. 2014, ApJ, 788, 28
Verhamme, A., Orlitová, I., Schaerer, D., et al. 2017, A&A, 597, A13
Weldon, A., Reddy, N. A., Topping, M. W., et al. 2022, MNRAS, 515, 841
Wisotzki, L., Bacon, R., Blaizot, J., et al. 2016, A&A, 587, A98
Wofford, A., Leitherer, C., & Salzer, J. 2013, ApJ, 765, 118
Xue, R., Lee, K.-S., Dey, A., et al. 2017, ApJ, 837, 172
Zackrisson, E., Inoue, A. K., & Jensen, H. 2013, ApJ, 777, 39
Zheng, Z., Cen, R., Weinberg, D., Trac, H., & Miralda-Escudé, J. 2011, ApJ,
```